$PdSe_2$: Pentagonal 2D Layers with High Air Stability for Electronics

Akinola D. Oyedele,[†,‡,#] Shize Yang,[⊥,#] Liangbo Liang,[‡,#] Alexander A. Puretzky,[‡] Kai Wang,[‡] Jingjie Zhang,[‡,§] Peng Yu,[ζ] Pushpa R. Pudasaini,[¶] Avik W. Ghosh,[§] Zheng Liu, [ζ] Christopher M. Rouleau,[‡] Bobby G. Sumpter,[‡] Matthew F. Chisholm, [⊥] Wu Zhou, [⊥] Philip D. Rack, [‡,¶] David B. Geohegan,[‡] Kai Xiao[‡,†,*]

[†]Bredesen Center for Interdisciplinary and Graduate Education, University of Tennessee, Knoxville, TN 37996, USA

[‡]Center for Nanophase Materials Sciences, Oak Ridge National Laboratory, Oak Ridge, Tennessee 37831, United States

[⊥]Materials Science and Technology Division, Oak Ridge National Laboratory, Oak Ridge, TN 37830, USA

[§]Department of Electrical and Computer Engineering, University of Virginia, Charlottesville, Virginia 22904, United States

[ζ]Center for Programmable Materials, School of Materials Science & Engineering, Nanyang Technological University, Singapore 639798, Singapore

[¶]Department of Materials Science and Engineering, University of Tennessee, Knoxville, Tennessee 37996, United States

KEYWORDS. Pentagonal, pucker, anisotropic, two-dimensional crystals, mobility.

ABSTRACT: Most studied two-dimensional (2D) materials exhibit isotropic behavior due to high lattice symmetry; however, lower-symmetry 2D materials such as phosphorene and other elemental 2D materials exhibit very interesting anisotropic properties. In this work, we report the atomic structure, electronic properties, and vibrational modes of few-layered $PdSe_2$, exfoliated from bulk crystals, a pentagonal 2D layered noble transition metal dichalcogenide with a puckered morphology that is air-stable. Micro-absorption optical spectroscopy and first-principles calculations reveal a wide band gap variation in this material from ~0 (bulk) to ~1.3 eV (monolayer). The Raman active vibrational modes of $PdSe_2$ were identified using polarized Raman spectroscopy, and the strong interlayer interaction was revealed from the large thickness-dependent Raman peak shifts, agreeing with first-principles Raman simulations. Field-effect transistors made from the few-layer $PdSe_2$ display tunable ambipolar charge carrier conduction with a high electron apparent field-effect mobility of ~158 $cm^2V^{-1}s^{-1}$, indicating the promise of this anisotropic, air-stable, pentagonal 2D material for 2D electronics.

INTRODUCTION

The emergence of two-dimensional (2D) crystals with unique structure and extraordinary electronic properties provides exciting opportunities for applications in nanoscale electronics.[1] For example, graphene has gained attention due to its high carrier mobility resulting from an effectively massless state of charge carriers,[2] but its inherent lack of a band gap, and the inability so far to induce a sizable one, limits its application in electronics. It would thus be desirable to realize a 2D system with a widely tunable band gap when targeting applications in nanoscale devices. This has led to the exploration of transition metal dichalcogenides (TMDs) and other 2D materials beyond graphene.[3] In this regard, MoS_2 has attracted the most attention because of its moderate mobility and high current on/off ratio in transistors, however, MoS_2 possesses a limited band gap variation between ~1.2 – 1.9 eV,[4-5]. Similarly, relatively new 2D Bi_2O_2Se system shows high electron mobility and high on/off ratio, but possesses a small bandgap of ~0.8 eV.[6-7] For electronic and photonic applications, a material that is air-stable and has high carrier mobility, high on/off ratio, as well as a more widely-tunable band gap is far more desirable.

Until the recent introduction of black phosphorus (BP), with a band gap variation from 0.3 – 1.5 eV, materials with such a widely tunable band gap were difficult to find.[8] BP has a honeycomb network similar to graphene, but is strongly puckered (that is not ideally planar, but oscillate out-of-plane in a regular corrugated manner), rendering exotic properties of the in-plane anisotropic response to external stimulations, such as polarized light, electric field, applied strain.[9-11] These anisotropies have their origins rooted in the puckering of the hexagonal lattice structure, which provides a new degree of freedom to explore in 2D materials. Recently, other buckled or puckered 2D materials with hexagonal structure have been theoretically and experimentally reported in elemental 2D materials (also called Xenes) such as silicene, germanene, and stanene.[12-13] In contrast with an isotropic planar hexagonal structure, the buckling breaks the sublattice symmetry, enhances spin-orbit coupling, and allows tuning of a topological quantum phase transition.[14] However, despite their potential importance for device applications, the realization of stable 2D buckled or puckered hexagonal structures of 2D elemental materials including BP, silicene, germanene, and stanene is still a great challenge for practical electronics. Furthermore, 2D materials with buckled or puckered *pentagonal* structure are another class of highly desirable 2D materials due to the low symmetry lattice structure. They have recently been theoretically predicted but have remained unexplored experimentally.[15-17] The pentagons are usually considered as topological de-

fects or geometrical frustrations as stated in the well-known "isolated pentagon rule" (IPR),[18] but rarely found as basic building blocks in 2D materials. Unlike the hexagonal structure as the dominant motifs in 2D materials, most of the predicted pentagonal 2D materials including penta-graphene and penta-SnS_2, are buckled or puckered in a regular corrugated manner to maintain symmetry. For example, pentagonal graphene presents a hybrid bond structure consisting of both sp^3 and sp^2 carbons, in a repeating pentagon arrangement. This unique atomic configuration coupled with the buckled structure results in a large band gap and exotic mechanical properties with an unusual negative Poisson's ratio and ultrahigh mechanical strength[15] which are interesting for flexible device applications. Also, penta-SnS_2 has been theoretically predicted to be a room temperature 2D quantum spin Hall (QSH) insulator with sizeable and nontrivial band gaps.[16] Therefore, 2D buckled pentagonal materials with low symmetry could open the possibility for future optoelectronic, piezoelectric, spintronic, and valleytronic applications. To the best of our knowledge, 2D materials composed of pentagonal structure have never been demonstrated experimentally.

Here, we demonstrate the isolation and characteristics of atomically thin palladium diselenide crystals with a novel puckered pentagonal structure, experimentally revealed by atomic-resolution scanning transmission electron microscopy. The puckered 2D $PdSe_2$ flakes exhibit a widely tunable band gap that varies from metallic (bulk) to ~1.3 eV (monolayer). Raman active modes in $PdSe_2$ were identified by polarized Raman spectroscopy and first-principles calculations, with a strong interlayer interaction in $PdSe_2$ revealed by the large, layer-dependent Raman peak shifts. Field-effect transistors made from the few-layer $PdSe_2$ display ambipolar charge carrier conduction with high electron field-effect mobility of ~ 158 $cm^2V^{-1}s^{-1}$. In addition, few layer $PdSe_2$ systems exhibit a metal-insulator transition (MIT), which is absent in bulk $PdSe_2$. Unlike BP, $PdSe_2$ is air-stable and can be synthesized potentially via chemical vapor deposition, which makes it an excellent candidate for practical electronics. Overall, our results indicate that 2D pentagonal materials should be useful in designing novel electronic devices that combine the charge, spin, and other degrees of freedom resulting from the low symmetry to achieve better performance and unprecedented functionalities.

EXPERIMETNAL DETAILS

Synthesis of bulk $PdSe_2$ crystals and exfoliation, Bulk $PdSe_2$ single crystals were grown by a self-flux method through melting stoichiometric amounts of Pd powder (99.98%, Alfa Aesar) and Se powder (99.94%, Alfa Aesar). The Pd and Se powders in an atomic ratio of Pd : Se = 1 : 6 were thoroughly mixed together and sealed in an evacuated quartz ampoule under a vacuum condition of 10^{-6} Torr and then placed in a one-zone thermal furnace. The furnace was slowly heated up to 850 °C and held for 50 hrs and then allowed to cool to 450 °C at a rate of 3 °C/hr, followed by cooling down to room temperature. Shiny single crystals of $PdSe_2$ were obtained by cleaving the ingot, i.e., the product, which is composed of the $PdSe_2$ flakes. Monolayer and few layer $PdSe_2$ flakes were prepared by micromechanical exfoliation of bulk crystals. For optical, morphological and device characterizations, clean silicon substrates with 280 nm SiO_2 layer were used to support the flakes. For STEM characterization, the $PdSe_2$ flakes were transferred from the SiO_2 substrates to the TEM grid via wet KOH/PMMA transfer method.[19] The flakes were directly exfoliated onto a 0.5 mm-thick commercially-available quartz substrate for absorption spectroscopy measurements.

STEM characterization Thin $PdSe_2$ flakes were first prepared by mechanical exfoliation onto a SiO_2 substrate, and then transferred with PMMA to a Quantifoil gold TEM grids using a 0.25 M KOH solution to dissolve the SiO_2. The samples were baked at 150 ^{0}C in vacuum before STEM observation. The medium angle annular dark field images (MAADF) were obtained using a Nion UltraSTEM100 microscope operated at 60 kV. The convergence angle of the electron beam is 30 mrad, and the inner detector half-angle used for HAADF and MAADF images were 71 and 50 mrad, respectively. The images presented in the paper are filtered using a Gaussian function with a FWHM of 0.12 nm.

DFT Calculations Plane-wave density functional theory (DFT) calculations were performed using the VASP package equipped with the projector-augmented-wave (PAW) method for electron-ion interactions.[20] The exchange-correlation interactions were considered in the generalized gradient approximation (GGA) using the Perdew-Burke-Ernzerhof (PBE) functional.[21] Van der Waals (vdW) interactions between the $PdSe_2$ layers were included using the vdW density functional method optPBE-vdW (denoted as optPBE).[22] For bulk $PdSe_2$, both atoms and cell volume were allowed to relax (i.e., ISIF = 3) until the residual forces were below 0.001 eV/Å, with a cutoff energy of 350 eV and the 12×12×8 k-point sampling. The optimized bulk lattice constants obtained via optPBE are a=5.85 Å, b=5.99 Å and c=7.95 Å, in good agreement with the experimental values (a=5.75 Å, b=5.87 Å and c=7.69 Å).[23-24] Note that the out-of-plane direction is defined as the *z*-axis. Based on the fully relaxed geometries, the dynamic matrix was then calculated using the finite difference scheme implemented in the Phonopy software to obtain phonon frequencies and eigenvectors. Raman intensity calculations were then performed within the Placzek approximation using an in-house developed Raman modeling package. More details about DFT calculations are in SI.

Device Fabrication and Measurement $PdSe_2$ crystals were exfoliated onto a silicon substrate with 280 nm thickness of SiO_2 layer. The location of suitable flakes was identified using a Nikon LV150 high-powered optical microscopy. AFM was performed to ascertain the thickness of the flakes. Electron beam lithography (FEI DB-FIB with Raith pattern software) was used for device fabrication. The metal contacts for the flakes, 5 nm of Ti followed by 30 nm Au, were deposited in vacuum using an electron beam evaporator. The FET device measurements were conducted using a Keithley 4200 semiconductor analyzer in a two-terminal configuration.

RESULTS AND DISCUSSION

Bulk $PdSe_2$ is a semimetal noble transition metal dichalcogenide that was theoretically predicted recently to have a unique pentagonal structure in 2D layers, with strong interlayer coupling and an extraordinary high carrier mobility.[24-26] As shown by the side view and projected top view of a 2D $PdSe_2$ monolayer in Figure 1 (b), it consists entirely of pentagonal rings with the vertices in a slightly asymmetrical boat conformation, which is similar to the puckered structure of BP (Figure 1(a)) but with hexagonal rings.[27] As shown in the figure, each Pd atom binds to four Se atoms in the same layer, and two neighboring Se atoms can form a covalent Se-Se bond.[28] To our knowledge, this pentagonal conformation has not yet been reported for any 2D materials structure, including graphene, other elemental 2D materials (also called Xenes), and TMDs.

Bulk $PdSe_2$ single crystals were grown by melting stoichiometric amounts of Pd powder and Se powder in an evacuated quartz ampoule under a vacuum condition of 10^{-6} Torr. The as-grown crystals are plate-like with a thickness around 4 mm. As shown in Figure 1(c) and Figure S1, bulk $PdSe_2$ displays Pbca symmetry (point group D_{2h}) with an orthorhombic lattice that contains four Pd and eight Se atoms in one unit cell.[28] The structure is made up of single layers of $PdSe_2$ stacking along the c-axis and held together mainly by van der Waals forces. From the top view, we can see that the monolayer $PdSe_2$ crystals are composed entirely of pentagonal rings, presenting an intriguing pattern that is known as the Cairo

pentagonal tiling.[15] This unique pentagonal structure has been predicted theoretically to be stable only for graphene and a few other 2D materials.[15-17]. In contrast to the structure of hexagonal 2D materials such as graphene, Xenes, and TMDs that have been reported experimentally, the $PdSe_2$ monolayer structure

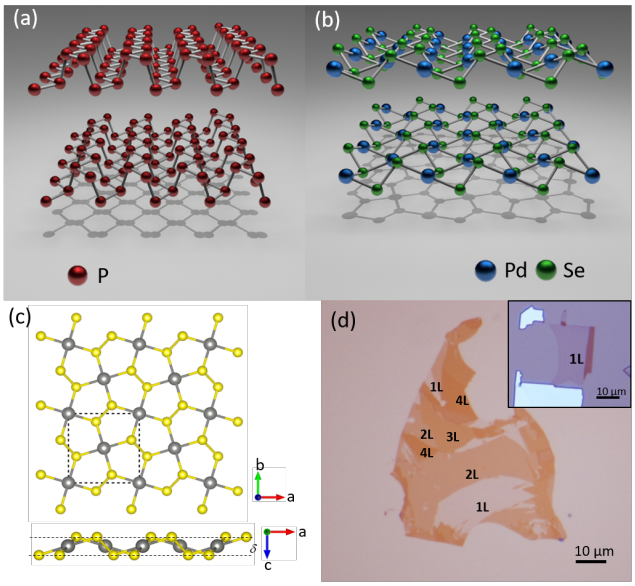

Figure 1. Crystallographic structure of 2D puckered (a) hexagonal black phosphorus and (b) pentagonal $PdSe_2$. (c) Top and side view of the crystal structure of monolayer $PdSe_2$ showing a puckered pentagonal configuration. The gray spheres represent the Pd atoms, while the yellow spheres represent the Se atoms. Dashed line indicates the unit cell. The vertical puckering distance, δ, is around ~1.6 Å (d) Optical image (OM) of exfoliated monolayer and few-layer $PdSe_2$ flakes on silicon substrate with 300 nm SiO_2 layer. The layer numbers were estimated from associated AFM measurements. Inset shows a large monolayer $PdSe_2$ flakes.

features unusual planar tetra-coordination of its Pd atoms, puckered pentagons with a vertical puckering distance, δ, of ~1.6Å, as well as Se–Se bonds. Although the predicted interlayer binding energy of $PdSe_2$ (190 meV/ atom)[24] is significantly higher than that of BP (40 meV/atom)[25], $PdSe_2$ mono- and few-layers were able to be isolated using micromechanical exfoliation by adhesive tapes, and as shown in Figure 1(d), large areas (~30 μm) were obtained. The thickness of the monolayer crystals was verified from atomic force microscopy (AFM) to be ~0.6 nm as shown in Figure S2. The thickness of multilayered $PdSe_2$ crystals was inferred from AFM measurements, and cross-calibrated by micro-Raman and micro-absorption spectroscopies as discussed in the SI. Interestingly, $PdSe_2$ exfoliates primarily into regular rectangular shapes, allowing the identification of it crystalline orientation (see Figure S2). As shown in Figure S3, the dynamical stability of the single and few-layer $PdSe_2$ is confirmed by the absence of soft modes in the calculated phonon dispersions. Note that very small negative frequencies are still present in the calculated phonon dispersion of monolayer $PdSe_2$, but by switching to the LDA functional they can be nearly eliminated, suggesting that such negative frequencies are likely due to the computational error.

The atomic structure of the $PdSe_2$ flakes was characterized by scanning transmission electron microscopy (STEM). Although we can exfoliate large monolayer $PdSe_2$ flakes onto a substrate and transfer it onto a TEM grid, it is hard to distinguish the pentagonal structure in the annular dark-field (ADF) image (Figure S4) due to the surrounding disordered region of the flakes, perhaps resulting from damage during transfer. Figure 2 shows the ADF image of few layer $PdSe_2$ crystals, and although, even and odd layer numbers appear very different in ADF as shown in Figure 2(a) and (b) due to symmetry differences, the patterns agree very well with the image simulations[22] shown in Fig. 2(c) and (d), respectively. Bulk $PdSe_2$ crystals exhibit space group Pbca space group symmetry and D_{2h} point group symmetry. In contrast, thin flakes with either an odd or even number of layers belong to space group $P2_1/c$ (No. 14) and point group C_{2h} (2/m) with inversion symmetry or space group $Pca2_1$ (No. 29) and point group C_{2v} (mm2) without inversion symmetry, respectively. The corresponding fast Fourier transform (FFT) patterns of few layer $PdSe_2$ in Figure S5 (a-c) show the rectangular structure distinct from the hexagonal structure of other TMDs. Each flake has an identical lattice structure with similar diffraction patterns of (020) and (200), confirming the crystallinity of each flakes. Electron energy loss spectroscopy (EELS) of the few-layer $PdSe_2$ flakes (Fig. S5(d-e)) shows characteristic peaks of Pd N,M edges and Se M edges.

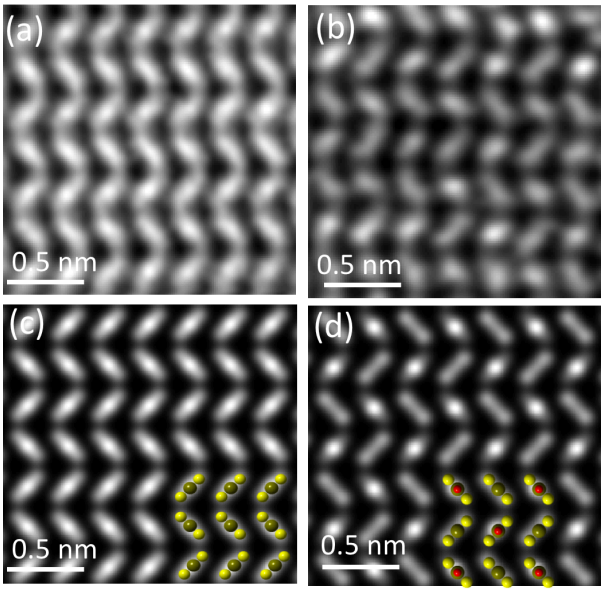

Figure 2. Atomic resolution structure of few-layer $PdSe_2$ crystals revealed by Z-contrast STEM images (top row) and corresponding simulated images (bottom row) of $PdSe_2$. (a, c) Even number of layers, (b, d) odd number of layers. Insets in c, d show atomic models of the corresponding STEM images.

According to the calculated electronic band structures in Figures 3(a) and 3(b), 1L $PdSe_2$ exhibits 1.3 eV indirect band gap and no band gap for the bulk. The 1.3 eV indirect band gap for a monolayer is quite close to its direct band gap (1.43 eV), making the $PdSe_2$ monolayer promising for optoelectronic applications. Similar indirect band gaps are observed in few-layer $PdSe_2$ as well (more details in Figure S6 in SI), indicating the intrinsic nature of this indirect band gap semiconductor compared to the indirect-to-direct band gap transition observed in other TMDs.[5] Generally speaking, the valence band maximum (VBM) is located between the high-symmetry Γ and X (0.5, 0, 0) points while the conduction band minimum (CBM) is located between Γ and M (0.38, 0.5, 0) points, suggesting that it is not located along the high-symmetry lines like the commonly studied TMDs (MoS_2 family)[3] and BP.[29] For the $PdSe_2$ systems, both the valence band edge and conduction band edge are contributed mostly by the Pd *4d*-states and Se *4p*-states, which indicates the energy levels of both VBM and CBM (thus the band gap) are sensitive to the interlayer coupling and electronic hybridization.[24] The inset of Figure 3b shows the rectangular shape of the first Brillouin zone of $PdSe_2$ 2D crystals. To determine the thickness dependence of the indirect band gap, optical absorption measurements were carried out and Tauc plots were used to derive the band gaps from the absorption spectra as shown in Figure

S7(d-g). Figure 3c shows the optical band gaps versus the number of $PdSe_2$ layers. The large uncertainty in the band gaps (±0.2 eV) can be explained by possible high amount of defects in the $PdSe_2$ flakes. Another possible source of this uncertainty may be related to in-plane anisotropic absorption properties of $PdSe_2$[17]. However, this data shows a clear trend of decreasing band gap with increasing number of layers from ~1.3 eV (1L) to 0 eV (bulk) (within the uncertainty of ±0.2 eV). This trend is consistent with the first-principle calculations (Figure 3(d)), although, the calculated band gap is generally smaller than experimental one because DFT tends to underestimate the band gap due to its limitation to describe the long-range many-body interactions. Therefore, the experimentally observed bang gap dependence for the thicker layers may reflect the importance of the many-body effects. Therefore, both our absorption measurements and DFT calculations show a layer-dependent band gap that changes approximately from 0 eV (bulk) to 1.3 eV (monolayer). Note that the changes of the $PdSe_2$ band gap from bulk to monolayer are noticeably larger than those for MoS_2.[5] Since Pd has more valence electrons than Mo (10 versus 6), it is expected that interlayer Pd and Se atoms are more hybridized, and that the interlayer coupling is stronger in this case.[24] This effect contributes to the strong layer-dependent band gaps for $PdSe_2$ and also for $PtS(Se)_2$ within the same group.[30-31]

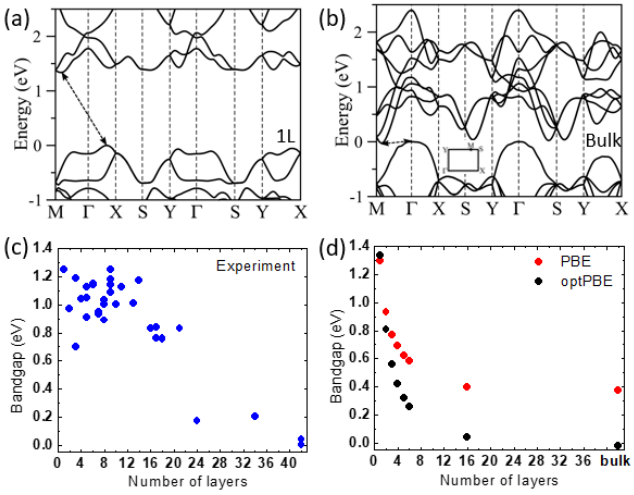

Figure 3. Calculated electronic band structures of (a) 1L and (b) bulk $PdSe_2$ by the optPBE method. The dashed arrows indicate the lowest energy transitions between the valence band maximum (VBM) and conduction band minimum (CBM). The VBM is set at 0 eV. Inset in (b) shows the Brillouin zones of $PdSe_2$ 2D crystals with high-symmetry points labeled (c) Band gaps extracted from the Tauc plots for various number of $PdSe_2$ layers derived from the optical absorption spectra (See Fig. S7 in SI for more details) (d) Band gaps obtained from first-principles calculations - PBE and optPBE shown in red and black dots, respectively.

As shown in Figure 1(c), the unit cell of bulk $PdSe_2$ is orthorhombic with space group *Pbca* (No. 61, point group D_{2h}).[28] Unlike most well-studied hexagonal TMDs such as MoS_2,[5] the symmetry of bulk $PdSe_2$ is comparable to BP, which is also orthorhombic (space group No. 64, point group D_{2h}).[32] As a result, symmetry assignments of phonon modes for $PdSe_2$ resemble those for BP, and this indicates that 2D $PdSe_2$ flakes should have unique anisotropy due to their in-plane low symmetry. The unit cell of bulk $PdSe_2$ consists of two layers and 12 atoms, and thus there are normal phonon modes at the Γ point whose irreducible representations are:

$$\Gamma_{bulk} = 3A_g + 3B_{1g} + 3B_{2g} + 3B_{3g} + 6A_u + 6B_{1u} + 6B_{2u} + 6B_{3u}, \quad (1)$$

where $3A_g$, $3B_{1g}$, $3B_{2g}$ and $3B_{3g}$ modes are Raman active. As shown in Figure 4(a), we find that only A_g and B_{1g} modes can be observed in our unpolarized Raman measurements (more details in SI). This is confirmed by the theoretical Raman spectra shown in Figure 4(b), where the bulk spectra (gray lines) exhibit five peaks. Although bulk $PdSe_2$ has 3 A_g modes (A_g^1, A_g^2, A_g^3) and 3 B_{1g} modes (B_{1g}^1, B_{1g}^2, B_{1g}^3), our calculations found that the A_g^1 and B_{1g}^1 modes are very close to each other with a frequency difference of less than 2 cm^{-1}, and subsequently a single mixed peak (denoted as A_g^1-B_{1g}^1) appears around 145 cm^{-1} according to the measurements (around 134 cm^{-1} according to the calculations). Detailed and strict symmetry assignments for all peaks are presented in Figure S8, but to further validate the peak symmetry assignments, polarized Raman measurements were carried out. As shown in Figure S9 in SI, in both the experimental and simulated polarized Raman spectra of $PdSe_2$, indeed only the three A_g peaks indeed appear under $\bar{z}(x,x)z$ while the three B_{1g} peaks appear under $\bar{z}(x,y)z$ because the A_g and B_{1g} modes have dramatically different response behaviors to laser polarization because of their different Raman tensors (more details in SI). The atomic vibrations of these six Raman modes are illustrated in Figure 4(c). This can be ascribed to the unique structure in $PdSe_2$ (Fig. 1(c)), in which each layer is actually a Se-Pd-Se trilayer with Pd atoms covalently bonded to four Se atoms on the top and bottom sublayers. It is interesting to point out that all of them mainly involve the vibrations of the Se atoms (blue arrows in Figure 4(c)). It is also interesting to note that all five Raman peaks generally shift to higher frequency with the thickness reduction from bulk to 1L. Figure 4(d) shows both the experimental (black) and theoretical (red) frequencies of the A_g^1-B_{1g}^1, B_{1g}^2, and A_g^3 peaks at different thicknesses. Although the calculated frequencies are systematically smaller than the experimental ones (by about 9-20 cm^{-1}), the trend of the frequency versus thickness is in agreement. In addition, the significant shifts of Raman peaks around 5-9 cm^{-1} from bulk to 1L for $PdSe_2$ are observed, which is different from the small shifts around 3-5 cm^{-1} observed in MoS_2.[33] This anomalous shift behavior is attributed to the strong interlayer coupling and hybridization in $PdSe_2$, which also leads to the wide band gap variation as we discussed above. Our calculations also indicate that the in-plane lattice constants decrease with decreasing thickness because of the strong interlayer interaction in $PdSe_2$. For instance, the in-plane lattice parameters, a and b, are reduced by ~2% and ~1%, respectively, going from bulk to 1L $PdSe_2$. Such a lattice contraction can stiffen the bonds and enhance the restoring forces (we refer to this as the "lattice shrinking effect"), which is one of the main factors responsible for the increasing peak frequencies from bulk to 1L (more details in SI).

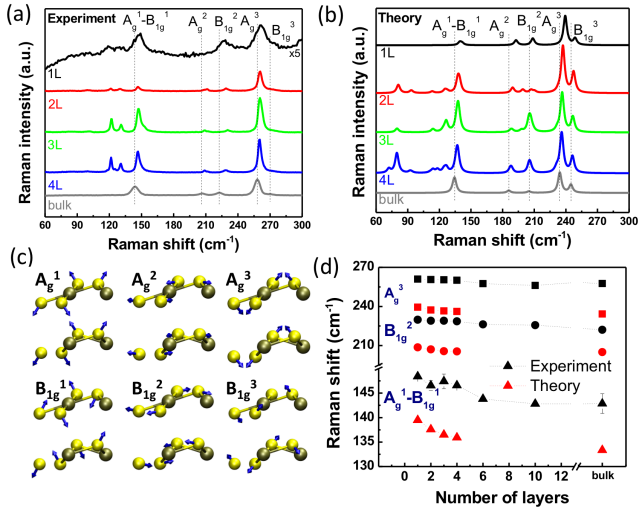

Figure 4. (a) Layer-dependent Raman spectra of $PdSe_2$ from 1L to bulk measured for an excitation laser wavelength of 532 nm. (b) Corresponding calculated Raman spectra by the optPBE method. In both (a) and (b), the dashed lines indicate positions of the Raman

peaks for bulk $PdSe_2$. Note that the A_g^1-B_{1g}^1 label means the overlapping of two close peaks: A_g^1 and B_{1g}^1. For convenience, bulk notations of A_g and B_{1g} are also used for other systems. (c) Atomic displacements (blue arrows) of six Raman modes in bulk $PdSe_2$. (d) Comparison of the experimental (black) and theoretical (red) frequencies of Raman modes A_g^1-B_{1g}^1, B_{1g}^2 and A_g^3 at different thicknesses. Although the calculated frequencies are systematically smaller than the experimental ones, the trend of the frequency shift versus thickness agrees.

To investigate the transport properties of 2D $PdSe_2$, field-effect transistor (FET) devices were fabricated using a two-terminal, back-gate configuration. Figure 5(a) shows the plot of the drain current (I_{ds}) as a function of back gate voltage (V_{bg}) for a typical 5L $PdSe_2$ device with 1.0 V drain bias. The linear behavior of the I_{ds}-V_{ds} characteristics shown in Figure S10(a-b) indicates good Ohmic contact. The device exhibits ambipolar transport with a slight asymmetry between holes and electrons. For this ~5 L device, electron apparent field-effect mobility as high as 70 $cm^2V^{-1}s^{-1}$ was achieved at room temperature and an on/off ratio greater than 10^5. Overall, we found higher mobilities for the electron carriers as compared with holes. To elucidate the layer-dependent electrical properties of 2D $PdSe_2$ crystals, the transfer characteristics for different number of layers of $PdSe_2$ is measured and shown in Figure S10(c). We observe distinct layer-dependent properties, in agreement with our optical characterization and electronic structure calculations. For example, as the number of layers increases, the gate control becomes negligible, which is consistent with a decrease in band gap. This is displayed in Figure 5(b), where the electron on/off ratio decreases from ~10^6, for bilayer $PdSe_2$, to ~10, for bulk $PdSe_2$. A Similar trend also can be observed for the on/off ratio for holes. The low on/off ratio (< 10) observed in bulk $PdSe_2$ can be associated with a quasi-metallic behavior. While the on/off ratio decreases monotonically as the number of layers is increased, the electron mobility peaks at ~20 L, similar to that observed in BP.[34] The statistical analysis for the mobility and on/off ratios of our ~65 devices are presented in the SI, showing an average electron mobility of ~80 $cm^2V^{-1}s^{-1}$ with a high of ~158 $cm^2V^{-1}s^{-1}$ (see Figure S11 in SI). Note that these values were measured without any materials treatment or device optimization, so perhaps with further device engineering, mobilities approaching the theoretical predicted value should be expected due to the low effective mass of noble transition metal dichalcogenides.[26] Interestingly, the $PdSe_2$ devices maintained their typical ambipolar behavior irrespective of the number of layers, with more symmetrical ambipolar behavior with increasing number of layers, which is very promising for high performance 2D logic circuits. The layer-dependence of the semiconductor-to-quasi-metal transition in $PdSe_2$ is also promising for fabricating single-material logic junction devices using 2D $PdSe_2$ crystals for both the channel and contact. This would eliminate the contact resistance due to scattering and Schottky barriers at the contact interface with the semiconducting channel.[35] It is important to note that unlike BPs, $PdSe_2$ remains stable (at least to 60 days for the present measurements) after exposure to air as shown in Figure S12.

The temperature dependence of the carrier mobility in 10 L $PdSe_2$ flakes shown in Figure 5(c) shows behavior similar to that found in other layered materials; the carrier mobility decreases at temperatures higher than ~100 K and saturates (or decrease slightly) at lower temperature. The behavior of the mobility at low temperature is most likely due to the dominant charged impurity scattering mechanism. As the temperature increases, the mobility decreases due to phonon scattering, following a power law relation $\mu \sim T^{-\gamma}$, where γ is close to 0.24. The γ value for few layer $PdSe_2$

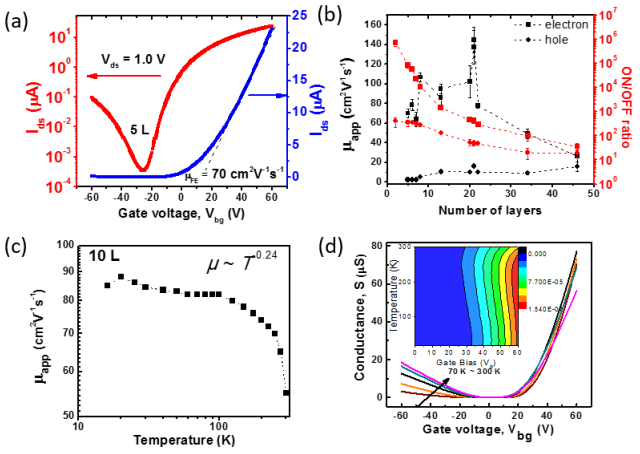

Figure 5. (a) Transfer curve of a typical ~5 layers $PdSe_2$ device, with both logarithmic and linear scales, showing ambipolar characteristics (b) Electron and hole apparent mobility, and on/off ratio versus flakes thickness for $PdSe_2$ devices measured at room temperature. Black line indicates mobility curve, while red line indicates on/off ratio curves. Data points in squares and circles represents electron and holes, respectively. The electron mobilities are higher than hole mobilities, and thicker films consistently show lower on/off ratio than that of thinner flakes. (c) The electron apparent mobilities measured at different temperatures for $PdSe_2$ flakes with a thickness of 10 layers. Below 100 K, the mobilities are independent of temperature, but above 100 K, the mobilities decrease with increasing temperature due to the phonon scattering, following a $T^{-\gamma}$ dependence with γ close to 0.24. (d) Conductance as a function of gate voltage for different temperatures for $PdSe_2$ flakes with a thickness of 10 layers. The crossing around ~40 V indicate the change in temperature dependence. Inset shows the color plot of the conductance as a function of temperature and gate bias.

is notably smaller than values in other 2D materials such as monolayer MoS_2 ($\gamma \approx 1.40$; ref. [36]), but agrees with that in few layer BP ($\gamma \approx 0.5$; ref. [9]) and monolayer MoS_2 with double dielectric layers ($\gamma \approx 0.3$; ref.[37]). The decrease in the value of γ may be attributed to the suppression of the homopolar phonon modes due to the strong interlayer interaction in layered $PdSe_2$. Further theoretical and experimental work is needed to clarify the detailed mechanism. In addition, an increase in current modulation up to $>10^9$ is observed for few-layer $PdSe_2$ as temperature is lowered (see Figure S13). The plot of the temperature dependence of the two-terminal conductivity at different gate bias for the 10 L device is shown in Figure S14. With $V_{bg} < 40$ V, the conductivity of the 10 L device decreases with decreasing temperature, indicating insulating behavior, whereas for $V_{bg} > 40$ V, the temperature dependence is reversed, showing metallic behavior. The crossover from insulating to metallic conductance is shown in more detail in Figure 5(d). Interestingly, this gate-bias induced metal-insulator transition (MIT) behavior was only observed in our thinner devices (i.e., <24 L). For thicker $PdSe_2$ devices, the conductance always increases with increased temperature at all gate bias (Figure S15) suggesting there is no MIT in thick flakes of $PdSe_2$. This MIT behavior could be a result of quantum interference effects of weak and strong localization (more discussion in SI).

CONCLUSIONS

In summary, we have successfully fabricated and characterized few-layer $PdSe_2$ crystals, a new member of the 2D materials family. 2D $PdSe_2$ exhibits an anisotropically puckered pentagonal structure that was revealed by atomic-resolution scanning transmission electron microscopy. The micro-absorption spectroscopy and first-

principles band structure calculations showed a wide band gap variation from ~0 (bulk) to ~1.3 eV (monolayer) in this material. Few-layer $PdSe_2$ devices exhibited excellent ambipolar semiconducting behavior with high room temperature electron apparent field-effect mobility (up to 158 $cm^2V^{-1}s^{-1}$). The Raman active modes in $PdSe_2$ were identified by polarized Raman spectroscopy and first-principles calculations, and strong interlayer interactions was revealed from the large layer-dependent Raman peak shifts. In addition, in-plane anisotropic properties should be expected for this highly anisotropic material because of the low in-plane symmetry structure. Temperature-dependent conductance measurements of few-layer $PdSe_2$ devices revealed that a metal-insulator transition behavior only exists in thin flakes. In addition, compared to other buckled or puckered 2D materials, such as BP, the 2D $PdSe_2$ exhibits much better air-stability (>60 days). Therefore, the discovery of new puckering pentagonal building blocks in 2D materials opens the possibility of both new emerging physics related to the low symmetry structure and various disruptive applications such as low-energy electronics, piezoelectrics, enhanced thermoelectricity and spintronics.

ASSOCIATED CONTENT

Supporting Information

The Supporting Information is available free of charge on the ACS Publications website.

Detailed descriptions of the characterizations, instrument parameters for the analytical techniques (AFM, Absorption and Raman spectroscopy, and FET), additional AFM, STEM, Raman, FET device performance, charge transport, and detailed theoretical calculation of the electronic structure, phonon spectrum, Raman spectrum. (PDF)

AUTHOR INFORMATION

Corresponding Author

* Kai Xiao, xiaok@ornl.gov

Author Contributions

[#]A.D.O., S.Y. and L.L. contributed equally to this work.

ACKNOWLEDGMENT

This research was conducted at the Center for Nanophase Materials Sciences (CNMS), which is a DOE Office of Science User Facility. A. O. acknowledges fellowship support from the UT/ORNL Bredesen Center for Interdisciplinary Research and Graduate Education. The single crystal growth (P. Y, Z. L) was supported by Singapore National Research Foundation under NRF RF Award No. NRF-RF2013-08. The electron microscopy (SZY, MFC, WZ) was supported by the Materials Science and Engineering Division, Office of Basic Energy Sciences, U.S. Department of Energy. This research used resources of the National Energy Research Scientific Computing Center, a DOE Office of Science User Facility. L. L. was supported by Eugene P. Wigner Fellowship at the Oak Ridge National Laboratory (ORNL). J. Z. was supported by Graduate Opportunities "GO!" program at ORNL. Part of the computations were performed using the resources of the Center for Computational Innovation at Rensselaer Polytechnic Institute. PRP and PDR acknowledge support by US Department of Energy (DOE) under Grant No. DOE DE-SC0002136.

REFERENCES

1. Novoselov, K.; Mishchenko, A.; Carvalho, A.; Neto, A. C. Science 2016, 353 (6298), aac9439.
2. Novoselov, K. S.; Fal, V.; Colombo, L.; Gellert, P.; Schwab, M.; Kim, K. Nature 2012, 490 (7419), 192-200.
3. Wang, Q. H.; Kalantar-Zadeh, K.; Kis, A.; Coleman, J. N.; Strano, M. S. Nature nanotechnology 2012, 7 (11), 699-712.
4. Radisavljevic, B.; Radenovic, A.; Brivio, J.; Giacometti, i. V.; Kis, A. Nature nanotechnology 2011, 6 (3), 147-150.
5. Mak, K. F.; Lee, C.; Hone, J.; Shan, J.; Heinz, T. F. Physical Review Letters 2010, 105 (13), 136805.
6. Wu, J.; Tan, C.; Tan, Z.; Liu, Y.; Yin, J.; Dang, W.; Wang, M.; Peng, H. Nano Letters 2017, 17 (5), 3021-3026.
7. Wu, J.; Yuan, H.; Meng, M.; Chen, C.; Sun, Y.; Chen, Z.; Dang, W.; Tan, C.; Liu, Y.; Yin, J. Nature Nanotechnology 2017, 12 (6), 530-534.
8. Li, L.; Yu, Y.; Ye, G. J.; Ge, Q.; Ou, X.; Wu, H.; Feng, D.; Chen, X. H.; Zhang, Y. Nature nanotechnology 2014, 9 (5), 372-377.
9. Xia, F.; Wang, H.; Jia, Y. Nature communications 2014, 5, 4458.
10. He, J.; He, D.; Wang, Y.; Cui, Q.; Bellus, M. Z.; Chiu, H.-Y.; Zhao, H. ACS Nano 2015, 9 (6), 6436-6442.
11. Phaneuf-L'Heureux, A.-L.; Favron, A.; Germain, J.-F.; Lavoie, P.; Desjardins, P.; Leonelli, R.; Martel, R.; Francoeur, S. Nano Letters 2016, 16 (12), 7761-7767.
12. Tao, L.; Cinquanta, E.; Chiappe, D.; Grazianetti, C.; Fanciulli, M.; Dubey, M.; Molle, A.; Akinwande, D. Nature Nanotechnology 2015, 10 (3), 227-231.
13. Li, L.; Lu, S. z.; Pan, J.; Qin, Z.; Wang, Y. Q.; Wang, Y.; Cao, G. Y.; Du, S.; Gao, H. J. Advanced Materials 2014, 26 (28), 4820-4824.
14. Quhe, R.; Fei, R.; Liu, Q.; Zheng, J.; Li, H.; Xu, C.; Ni, Z.; Wang, Y.; Yu, D.; Gao, Z. Scientific Reports 2012, 2, 853.
15. Zhang, S.; Zhou, J.; Wang, Q.; Chen, X.; Kawazoe, Y.; Jena, P. Proceedings of the National Academy of Sciences 2015, 112 (8), 2372-2377.
16. Ma, Y.; Kou, L.; Li, X.; Dai, Y.; Heine, T. NPG Asia Materials 2016, 8 (4), e264.
17. Yagmurcukardes, M.; Sahin, H.; Kang, J.; Torun, E.; Peeters, F.; Senger, R. Journal of Applied Physics 2015, 118 (10), 104303.
18. Wang, X.-Q.; Li, H.-D.; Wang, J.-T. Physical Chemistry Chemical Physics 2013, 15 (6), 2024-2030.
19. Li, H.; Wu, J.; Huang, X.; Yin, Z.; Liu, J.; Zhang, H. ACS Nano 2014, 8 (7), 6563-6570.
20. Kresse, G.; Furthmüller, J. Computational Materials Science 1996, 6 (1), 15-50.
21. Perdew, J. P.; Burke, K.; Ernzerhof, M. Physical Review Letters 1996, 77 (18), 3865.
22. Dion, M.; Rydberg, H.; Schröder, E.; Langreth, D. C.; Lundqvist, B. I. Physical Review Letters 2004, 92 (24), 246401.
23. Soulard, C.; Rocquefelte, X.; Petit, P.-E.; Evain, M.; Jobic, S.; Itie, J.-P.; Munsch, P.; Koo, H.-J.; Whangbo, M.-H. Inorganic Chemistry 2004, 43 (6), 1943-1949.
24. Sun, J.; Shi, H.; Siegrist, T.; Singh, D. J. Applied Physics Letters 2015, 107 (15), 153902.
25. Wang, Y.; Li, Y.; Chen, Z. Journal of Materials Chemistry C 2015, 3 (37), 9603-9608.
26. Liu, X.; Zhou, H.; Yang, B.; Qu, Y.; Zhao, M. Scientific Reports 2017, 7, 39995.
27. Castellanos-Gomez, A.; Vicarelli, L.; Prada, E.; Island, J. O.; Narasimha-Acharya, K.; Blanter, S. I.; Groenendijk, D. J.; Buscema, M.; Steele, G. A.; Alvarez, J. 2D Materials 2014, 1 (2), 025001.
28. Grønvold, F.; Røst, E. Acta Crystallographica 1957, 10 (4), 329-331.
29. Tran, V.; Soklaski, R.; Liang, Y.; Yang, L. Physical Review B 2014, 89 (23), 235319.
30. Wang, Y.; Li, L.; Yao, W.; Song, S.; Sun, J.; Pan, J.; Ren, X.; Li, C.; Okunishi, E.; Wang, Y.-Q. Nano Letters 2015, 15 (6), 4013-4018.

31. Zhao, Y.; Qiao, J.; Yu, P.; Hu, Z.; Lin, Z.; Lau, S. P.; Liu, Z.; Ji, W.; Chai, Y. Advanced Materials 2016, 28, (12), 2399-2407.
32. Ling, X.; Liang, L.; Huang, S.; Puretzky, A. A.; Geohegan, D. B.; Sumpter, B. G.; Kong, J.; Meunier, V.; Dresselhaus, M. S. Nano Letters 2015, 15 (6), 4080-4088.
33. Li, H.; Zhang, Q.; Yap, C. C. R.; Tay, B. K.; Edwin, T. H. T.; Olivier, A.; Baillargeat, D. Advanced Functional Materials 2012, 22 (7), 1385-1390.
34. Liu, H.; Neal, A. T.; Zhu, Z.; Luo, Z.; Xu, X.; Tománek, D.; Ye, P. D. ACS Nano 2014, 8 (4), 4033-4041.
35. Allain, A.; Kang, J.; Banerjee, K.; Kis, A. Nature Materials 2015, 14 (12), 1195-1205.
36. Radisavljevic, B.; Kis, A. Nature materials 2013, 12 (9), 815-820.
37. Lin, M.-W.; Kravchenko, I. I.; Fowlkes, J.; Li, X.; Puretzky, A. A.; Rouleau, C. M.; Geohegan, D. B.; Xiao, K. Nanotechnology 2016, 27 (16), 165203.

TOC Figure